Geophysical Prospecting

EAGE EUROPEAN ASSOCIATION OF GEOSCIENTISTS & ENGINEERS

Geophysical Prospecting, 2010, **58**, 1159–1176 doi: 10.1111/j.1365-2478.2010.00882.x

Multi-transient electromagnetic repeatability experiment over the North Sea Harding field‡

Anton Ziolkowski[1*§], Ronnie Parr[2], David Wright[1§], Victoria Nockles[3], Christopher Limond[4§], Ed Morris[3] and Jonathan Linfoot[3]

[1]*University of Edinburgh, Grant Institute, West Mains Road, Edinburgh EH9 3JW, UK,* [2]*BP, Burnside Industrial Centre, Wellheads Rd, Farburn Industrial Estate, Dyce, Aberdeen AB21 7PB, UK,* [3]*PGS, Geoscience and Engineering, Birch House, 10 Bankhead Crossway South, Edinburgh EH11 4EP, UK, and* [4]*BP Exploration Operating Company Ltd, Compass Point, 79-87 Kingston Road, Staines TW18 1DY, UK*

Received October 2009, revision accepted February 2010

ABSTRACT

We present results of synthetic time-lapse and real repeatability multi-transient electromagnetic surveys over the North Sea Harding field. Using Archie's law to convert porosity and fluid saturation to resistivity we created 3D isotropic models of the reservoir resistivity at different stages of production from the initial state in 1996 through to complete hydrocarbon production by 2016 and, for each stage, we simulated an east-west transient electromagnetic survey line across Harding. Unconstrained 1D full-waveform Occam inversions of these synthetic data show that Harding should be detectable and its lateral extent reasonably well-defined. Resistivity changes caused by hydrocarbon production from initial pre-production state to production of the oil rim in 2011 are discernible as are significant changes from 2011–2016 during the modelled gas blowdown phase.

The 2D repeatability surveys of 2007 and 2008 tied two wells: one on and the other off the structure. Between the two surveys the segment of the field under investigation produced 3.9 million barrels of oil – not enough to generate an observable time-lapse electromagnetic anomaly with a signal-to-noise ratio of 40 dB. Processing of the 2007 and 2008 data included deconvolution for the measured source current and removal of spatially-correlated noise, which increased the signal-to-noise ratio of the recovered impulse responses by about 20 dB and resulted in a normalized root-mean-square difference of 3.9% between the data sets. 1D full-waveform Occam inversions of the real data showed that Harding was detectable and its lateral extent was also reasonably well-defined.

The results indicate that the multi-transient electromagnetic method is suitable for exploration, appraisal and monitoring hydrocarbon production.

Key words: Deconvolution, Electromagnetism (EM), Time-lapse.

INTRODUCTION

In 2007 and 2008 the North Sea Harding field was the focus of a time-lapse transient electromagnetic experiment conducted as part of a collaborative research project between MTEM Ltd (now PGS), BP and the UK Department of Trade and Industry (now UK Department for Business, Innovation and Skills) under project number H0531E. The principal

‡This paper is based on extended abstracts X006/Z036 presented at the 71st EAGE Conference & Exhibition Incorporating SPE EUROPEC 2009, 8–11 June 2009 in Amsterdam, the Netherlands.

*E-mail: anton.ziolkowski@pgs.com

§Formerly at: PGS, Geoscience and Engineering, Birch House, 10 Bankhead Crossway South, Edinburgh EH11 4EP, UK.

objectives of the experiment were 1) to evaluate the potential of the multi-transient electromagnetic (EM) method (Wright, Ziolkowski and Hobbs 2002, 2005; Ziolkowski, Hobbs and Wright 2007) for identifying resistive hydrocarbon-saturated reservoir compartments in sub-sea fields in water depths less than 200 m deep and 2) to determine the repeatability of the multi-transient electromagnetic method in a marine environment.

Figure 1 shows the location of Harding. It is a medium-size oil and gas field at a depth of about 1700 m below the sea floor in block 9/23B in the central North Sea, about 320 km north-east of Aberdeen. The field has a high net-to-gross, high quality, Eocene Balder sandstone reservoir. Original oil in place was 300 million barrels. First oil production was in 1996, with gas being re-injected into the reservoir. Oil production is now in decline – currently production is about 10 000 bbl per day with increasing water cut. The remaining hydrocarbon column consists of a gas cap of about 100 m vertical extent and a thin remaining oil rim of less than 20 m vertical extent.

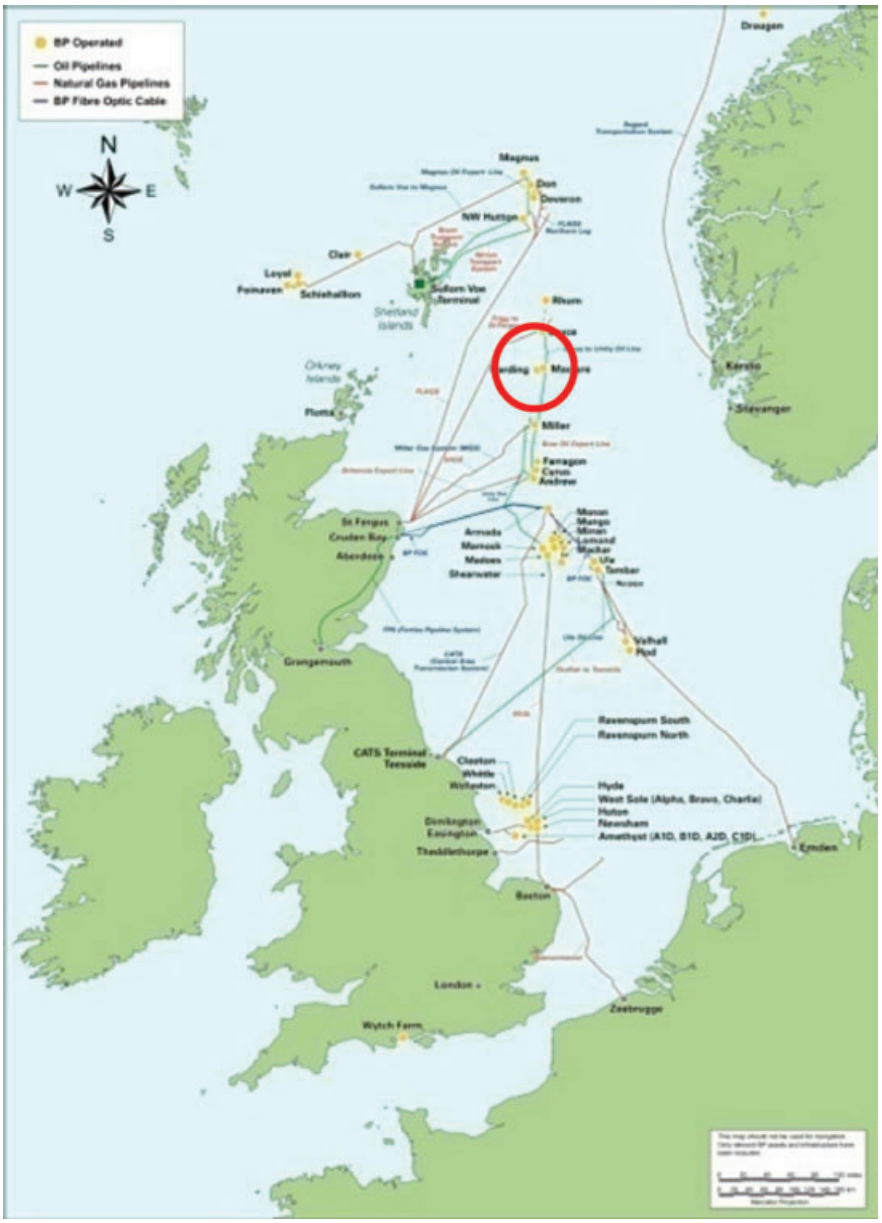

Figure 1 Map of the North Sea showing the position of the Harding field.

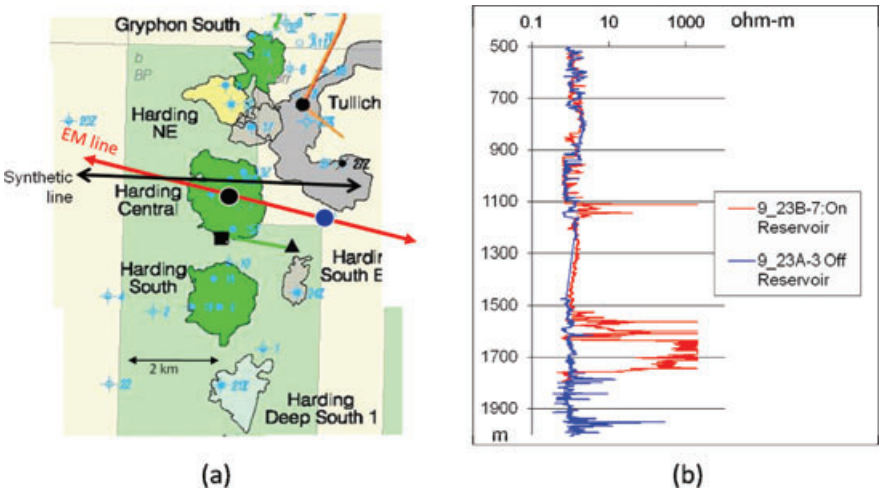

Figure 2 Showing position of the EM line relative to Harding Central field. a) The EM survey line in red intersecting Harding Central, the on-structure well 9/23B-7 (the black dot) and the off-structure well 9/23A-3 (the blue dot); also shown is the black east-west line used for generating the synthetic data; b) resistivity logs of the two wells: on-structure well 9/23b-7, with resistivity values in excess of 1000 Ωm at the reservoir (1700 m) and off-structure well 9/23A-3, with resistivity values 1–3 Ωm in the target zone.

Figure 2(a) shows the position of the EM survey line relative to an outline of Harding Central, which is about 2 km across. The line was acquired to tie a well, 9/23B-7, across the thickest part of the hydrocarbon reservoir and a second well, 9/23A-3, which is outside closure and about 2.2 km to the east of 9/23B-7. The line was orientated away from platform infrastructure and production operations. The resistivity log of the on-structure well, shown in red in Fig. 2(b), shows values in excess of 1000 Ωm at the gas-bearing portion of the reservoir at 1700 m depth, while the resistivity log of the off-structure well, shown in blue in Fig. 2(b) shows typical North Sea young sediment values of 1–3 Ωm in the equivalent target zone.

To assess the feasibility of achieving the principal objectives we generated time-lapse synthetic transient EM data for different states of the reservoir, obtained from previous reservoir simulation, from the initial pre-production state in 1996, through the oil production phase to 2011 and finally through gas cap production to 2016. The position of the east-west line along which we computed the synthetic data is shown in Fig. 2(a). The 3D transient EM modelling described below showed that the Harding field should be detectable and its lateral extent should be well-defined. That is, the transient EM method should be usable for both exploration and appraisal.

Resistivity changes caused by hydrocarbon production from initial pre-production state to production of the oil rim in 2011 should also be discernible, as should more significant changes from 2011–2016 during the gas blowdown phase. That is, the method should also be usable to monitor hydrocarbon production over time.

Collated 1D inversions of the common-midpoint (CMP) gathers of the real measured transient EM data confirmed the detectability of Harding and confirmed that the lateral extent of the field was reasonably well-defined.

We describe the multi-transient EM method for the marine case and outline the procedures we developed for modelling and inversion of the transient EM data from the reservoir simulations. We describe the field experiment, detailing the acquisition, processing and inversion of the time-lapse transient EM data. Processing included an innovative step, developed within the project, to remove the spatially-correlated noise; this increased the signal-to-noise ratio of the recovered impulse responses by as much as 20 dB and has helped to make the future development of towed streamer EM data acquisition feasible.

MULTI-TRANSIENT ELECTROMAGNETIC METHOD

Figure 3 shows the setup used for the acquisition of marine multi-transient EM data. The objective was to obtain the Earth's impulse response for each source-receiver pair. The source was a horizontal electric current bipole of length 400 m deployed on the sea floor. It can transmit any programmable current signal within its bandwidth. We used a signal that changed polarity in a transient pseudo-random binary sequence and measured the actual transmitted current.

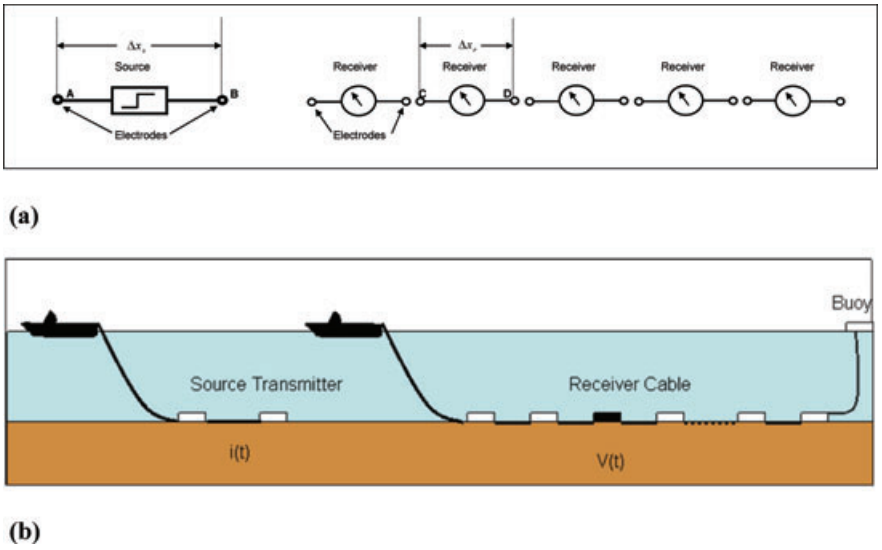

Figure 3 a) Plan view of a typical land MTEM source-receiver configuration, with a current bipole source and its two electrodes A and B and a line of receivers in-line with the source, measuring the potential between pairs of receiver electrodes, for instance C and D. b) Sectional view of one possible marine MTEM setup showing bipole source on the sea floor and separate receiver cable with bipole receivers, synchronized with GPS and with real-time quality control; typical bipole source and receiver lengths are 200 m.

A pseudo-random binary sequence has a flat amplitude spectrum over a given frequency bandwidth, which can be chosen to be the same as the bandwidth of the impulse response to be recovered (Wright, Ziolkowski and Hall 2006).

The in-line horizontal electric field response was measured by an in-line receiver cable consisting of up to 30 electric bipoles, each of length 200 m. The system provides real-time quality control of all the measurements. The measured voltage response at a receiver is

$$v(t) = \Delta x_r \Delta x_s i(t) * g(t) + n(t), \quad (1)$$

in which Δx_r is the length of the receiver bipole, Δx_s is the length of the source bipole, $i(t)$ is the input current, the asterisk $*$ denotes convolution, $g(t)$ is the impulse response of the Earth and $n(t)$ is noise uncorrelated with the signal: it is what would be measured if there was no signal emitted by the source. The measured voltage is deconvolved for the measured input current and divided by the measured source and receiver bipole lengths to recover the Earth impulse response, as described in detail by Ziolkowski *et al.* (2007). The process of deconvolution effectively compresses the source signal to a band-limited impulse: that is, all the energy of the long pseudo-random source signal is concentrated into a very small time interval. A pseudo-random binary sequence has properties that are ideal for this type of signal compression.

There is a separate impulse response for each source-receiver pair. The impulse responses are subsequently inverted for subsurface resistivity.

3D ELECTROMAGNETIC TIME-LAPSE MODELLING METHOD

Figure 2(a) shows a map of the Harding Central and Harding South fields, the real multi-transient EM survey line in red and the modelled survey line in black. The orientation of the real survey line was determined by the location of the two wells: 9/23B-7 on the Harding structure and 9/23A-3 off the structure and to the east.

The purpose of the modelling was not to generate an accurate simulation of the real data but to investigate the detectability of the reservoir. We were able to do this by simulating transient EM data along a line close to the survey line but in an east-west orientation. The integral equation 3D EM modelling code we used, known as Pie3D (Hursán and Zhdanov 2002), requires the source to be in one of the resistivity model Cartesian coordinate directions. The Cartesian coordinates of the resistivity model were based on the reservoir model, in which the grid was north-south and east-west. To simulate data exactly along the real survey line would have required the model to be rotated about a vertical axis to align the grid parallel and perpendicular to the real survey line. Since a direct comparison of modelled and real data was

not an object of the research, we decided to place the model survey line close to the real survey line, without rotating the reservoir model, such that the principal features of the data would be modelled correctly.

The Harding reservoir simulation model was converted for input to the Pie3D modelling code by the following process: 1) the reservoir model was converted to ASCII using commercially-available software; 2) the reservoir petrophysical properties, porosity and water saturation, were converted to resistivity in each cell using Archie's law; 3) the model was regridded in Matlab (a) to make the grid regular in x, y and z for ease of computation and (b) to reduce the number of cells and, consequently, the computation time and 4) the resulting model was converted for input to the Pie3D code. One, non-serious, limitation of the Pie3D code is that it does not work if the vertical dimension of the cells is too small. The vertical cell size used for reservoir modelling was much smaller than the resolution of the EM data. Increasing it to 6 m was sensible: it was still below the resolution of the EM data but it allowed the code to run.

A relation between petrophysical properties and resistivity was formulated for clean sands by Archie (1942). Modifications of Archie's law to include the presence of clay were proposed by DeWitte (1957) and Bussian (1983). Glover, Hole and Pous (2000) proposed a model in which each phase has its own connectivity. Core analysis showed the Balder sands at Harding to be clean, so Archies's law is appropriate to relate the petrophysical properties to the resistivity. Archie's law is:

$$\rho_t = \frac{a\rho_w}{\phi^m S_w^n}, \tag{2}$$

in which ρ_t is the total resistivity of the rock and contained fluid, ρ_w is the resistivity of the water in the rock, ϕ is the porosity, S_w is the saturation of the water and n, m and a are empirical numbers that were given the values 2, 2.02 and 0.845, respectively, based on recommendations by Hacikoylu, Dvorkin and Mavko (2006).

Inspection of equation (2) reveals that ρ_t tends to infinity as S_w tends to zero. Some cells in the reservoir model had very low values of water saturation S_w, which resulted in enormous values of resistivity ρ_t. Two questions arise: 1) can we decide whether very high resistivities (say, greater than 400 Ωm) are realistic, given the information available? and 2) does it actually matter? That is: is the modelling significantly affected by extremely high values of resistivity?

Addressing the first question, Fig. 2(b) shows that the log is saturated at 1200 Ωm so it is unreliable at high resistivities. A normal induction log measures conductivity rather than resistivity and its sensitivity decreases with decreasing conductivity (increasing resistivity). It is unable to distinguish between resistivities of 600 Ωm and 1200 Ωm, for example. So the correct resistivity value could take a wide range of values above, say, 400 Ωm. Another consideration is anisotropy. Ellis and Sinha (2009) explained that the magnetic induction measured in the induction log in a vertical borehole is for currents flowing in horizontal planes, whereas the vertical component of the current flow makes a larger contribution to the response in controlled source electromagnetic exploration with in-line horizontal electric bipole source and receivers. Using resistivity measurements in deviated wells Ellis and Sinha (2009) showed that resistivity is anisotropic, with the vertical resistivity being greater than the horizontal, in horizontal layers. Shales are much more anisotropic than sandstones, with vertical-to-horizontal resistivities up to about 5. We conclude that values of resistivity above, say, 400 Ωm are possible but we do not know how reliable they are.

To address the second question, we have computed the impulse response for a rectangular resistive body buried in a 1 Ωm half-space below a 110 m deep water layer with source and receiver on the sea floor, using the method of Hursán and Zhdanov (2002). In one specific case the body was at 1700 m below the sea floor, with dimensions 2 km in x by 2 km in y by 100 m in z, with its centre mid-way between source and receiver, which were 5 km apart. We made the resistivity of the body 400 Ωm. Since the resistivity of the background is 1 Ωm, the ratio of reservoir to background resistivities is 400. Increasing the resistivity of the body to 1200 Ωm increased the amplitude of the response by 0.36 per cent. In other words, the true values of the resistivities above about 400 Ωm are not important.

We know that the resistivity of the Harding dry gas reservoir is very high. Given the uncertainty of the true value of the resistivity, we decided to limit the maximum resistivity to the maximum value registered by the log: 1200 Ωm.

A horizontal slice through the Harding Central reservoir is shown in Fig. 4(a). The result of regridding is shown in Fig. 4(b). Since the computation time increases with the number of cells, the size of the regridded cells was chosen to be as large as possible, without producing a noticeable change in the modelled 3D response. Regridding gave a factor of 4 reduction in the number of cells.

The 3D model consisted of a water column 110 m deep with resistivity of 0.3 Ωm, overlying a uniform half-space of resistivity 1.0 Ωm, in which the 3D Harding resistivity model was embedded. Sections of the reservoir resistivity models are

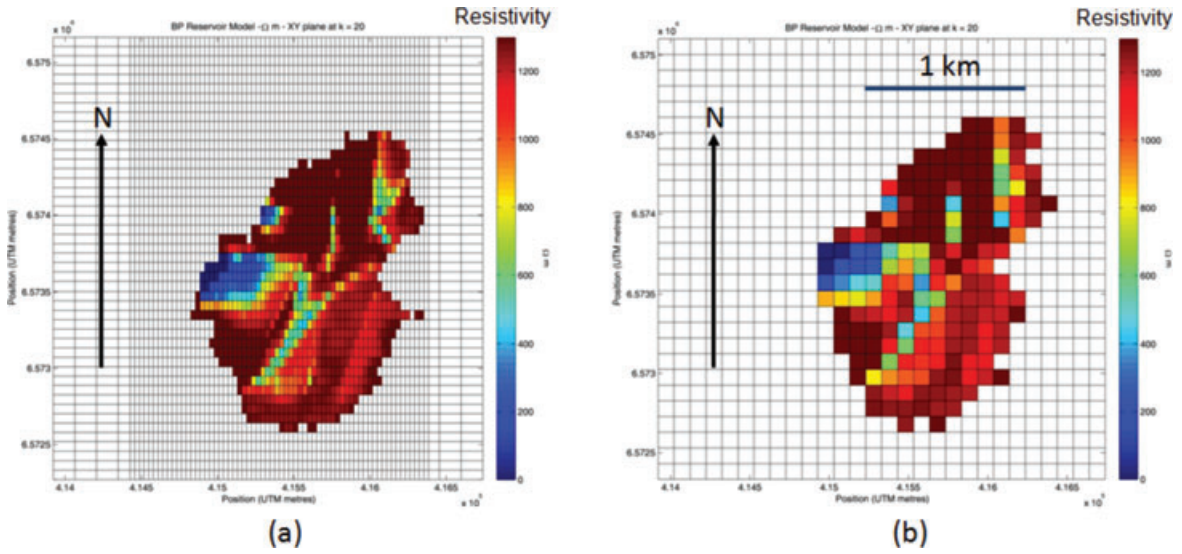

Figure 4 Horizontal slice through Harding Central showing resistivity variations: a) original reservoir mesh; b) re-gridded mesh.

shown in Fig. 5, for four times: initial state – 1996; January 2009; January 2011 – after production of the oil rim; and January 2016 – the modelled prediction of resistivity after gas cap production ('gas blowdown'). The maximum gas-saturated reservoir sandstone resistivity is 1200 Ωm, while the brine-saturated sandstone resistivity is 0.332 Ωm. The oil-saturated reservoir has intermediate resistivities; the variation in resistivity in the oil section is caused predominantly by saturation variations, with the water saturation S_W decreasing from the bottom of the section to the top. The gridding is 100 m in x (east-west), 100 m in y (north-south) and 6 m in z (vertical).

The initial state shows the gas overlying the oil, overlying the brine. Oil production from 1996 to January 2009 leaves only a 10 m rim of oil, with brine replacing oil and the gas cap remaining intact. From January 2009–2011 there is very little change, with oil production of less than 10 000 barrels per day. Gas cap production, 'gas blowdown', simulated between January 2011–2016, results in replacement of the bulk of the gas by brine sweeping up from the aquifer. Hydrocarbon production in this segment of Harding would be virtually complete by 2016.

TIME-LAPSE MODELLING RESULTS

For each snap-shot model, transient EM data were simulated with a grounded electric dipole on the sea floor and 30 in-line electric field receivers at 200 m intervals with source-receiver offsets of 2000–8000 m; the setup was moved along the line in steps of 400 m. Inversion of the synthetic data followed the method outlined in Ziolkowski *et al.* (2007). A one-dimensional (1D) Earth model was found to fit the impulse response data of each common-mid-point (CMP) gather using unconstrained full-waveform Occam inversion with a known, fixed, 110 m deep water layer of resistivity 0.3 Ωm overlying a 1 Ωm m half-space starting Earth model. The resulting 1D inversions are displayed side-by-side to give a 2D section of resistivity beneath the profile line. Figure 6 shows the inversion results for the four snap-shots: initial model; 2009; 2011; 2016. The colour scale is the same for all four results.

These inversions of the modelled data show that the field should be detectable, although the unconstrained Occam inversion puts the reservoir slightly shallower than the true position shown by the outline of the reservoir and the vertical resolution of the inverted resistivity model is poor. The lateral extent of the reservoir is reasonable.

By 'unconstrained' we mean that the water layer parameters are known and the starting model is a half-space. In this case the half-space resistivity was chosen to be 1.0 Ωm, which is exactly right everywhere except at the reservoir. The Occam inversion algorithm was described by Constable, Parker and Constable (1987). It allows the number of layers to be flexible but minimizes the rate of change of resistivity with depth, generating the smoothest model consistent with the data. This 'Occam regularization' is itself a kind of constraint. The procedure guards against severe oscillations that can occur if the layer thicknesses are chosen to be below the resolution of the

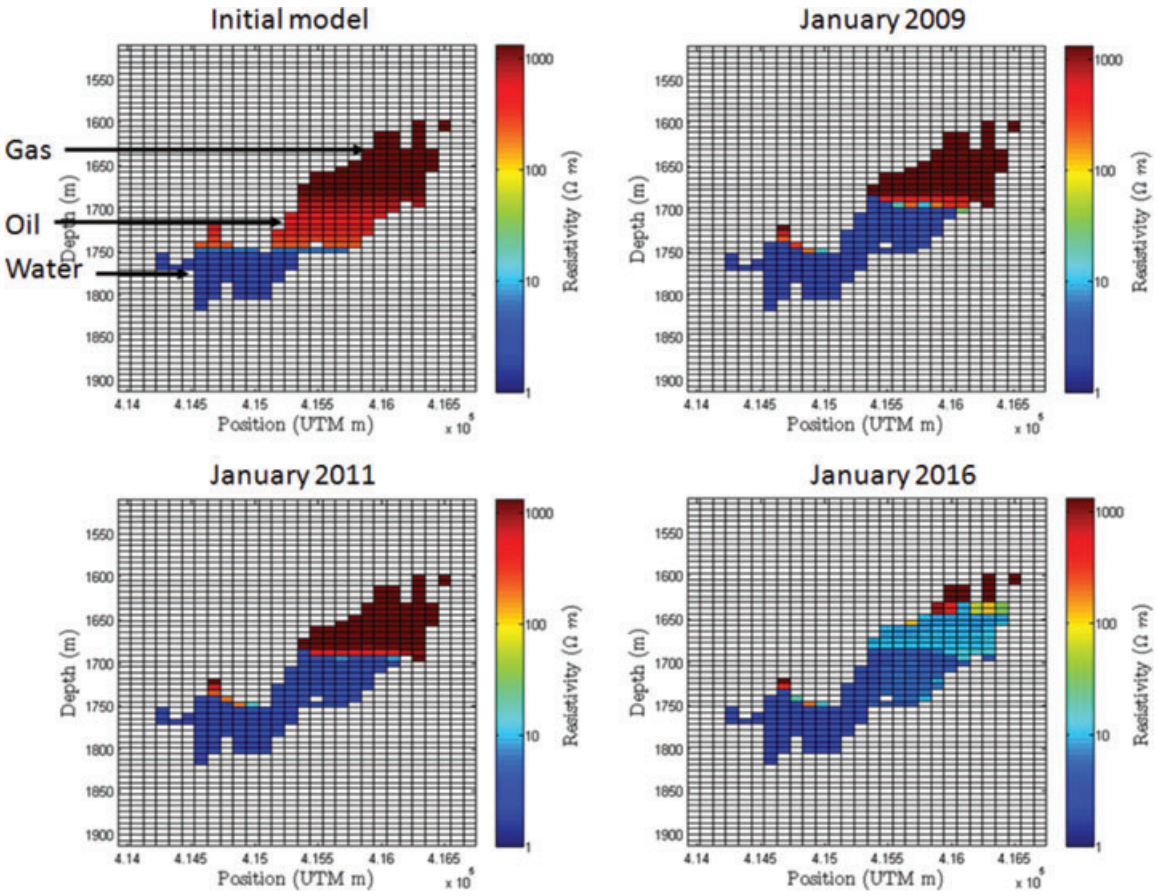

Figure 5 East-west resistivity sections at different times across Harding Central obtained from the reservoir simulation model using Archie's law. The vertical colour scale is logarithmic from 1 Ωm (bottom) to 1200 Ωm (top).

data. However, it can still leave minor artefacts in the presence of large resistivity contrasts.

Since the 1D inversion represents the reservoir as a layer with infinite extent in the *x*- and *y*-directions, it gives a very low estimate of the resistivity. Instead of 1200 Ωm at the reservoir in the initial model, we have resistivities around 1.5 Ωm, compared with the 1 Ωm background. As production of hydrocarbons proceeds, the amplitude of the reservoir response decreases and the inversion shows progressively lower resistivity from the target. The change from the initial state to 2009 as oil is produced is clearly observable as a decrease in amplitude; the change from 2009–2011 is very slight; and the change from 2011–2016 is again clearly observable, as the gas is produced.

Figure 7 shows relative percentage differences in the inversion results between the initial model and 2011 and between 2011 and 2016. These confirm what can be seen qualitatively in Fig. 6 but serious artefacts occur above and below the reservoir. These are caused first, by differences in the artefacts originating with the Occam inversion discussed above and, second, by the fundamental limitations of the 1D inversion that finds equivalent 1D low-resistivity resistors to represent the anomalies caused by finite 3D high-resistivity resistors. The artefacts are essentially caused by the differences in small numbers.

The 3D modelling and subsequent 1D inversions show that the transient EM method should be able to detect a medium-size field like Harding at about 1.7 km depth below water 100 m deep. The method can therefore be used for exploration. Since the method is also capable of providing a reasonable estimate of the lateral extent of the reservoir, it holds the promise of being able to appraise the extent of a discovered reservoir, or find additional compartments. Finally, the significant differences in amplitude with various stages of hydrocarbon production show that the method also has the potential to monitor production.

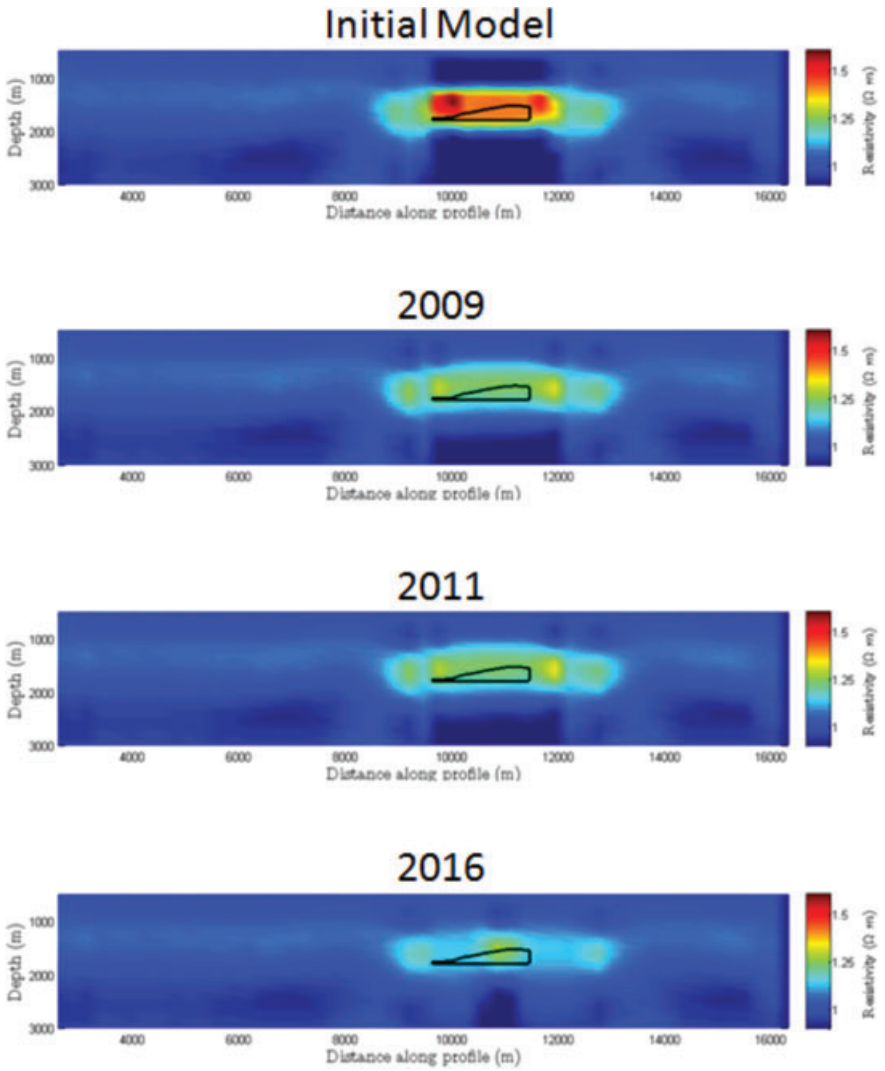

Figure 6 Collated 1D unconstrained depth inversion of CMP gathers of synthetic data for different time snap-shots. Vertical scale is depth in m; horizontal scale is horizontal position in m; the colour scale is linear in Ωm. The model reservoir is delineated by the black outline at 1700 m depth and 10 000–11 500 m on the horizontal axis.

FIELD EXPERIMENT OVER HARDING CENTRAL

Data acquisition

Figure 8 shows the subsurface coverage along the 10 km line for the original 20–22 October 2007 survey and the repeat survey of 27–31 August 2008. The configuration for the data acquisition was as follows. The receiver vessel laid the receiver cable from west to east and the source vessel positioned the receiver electrodes using acoustic transponders attached to the cable at the electrode positions. The source vessel then began at the eastern end of the cable, first at an offset of 4500 m and then at decreasing offsets, with a moveup of 400 m between successive source positions. At each source position transponders on the source electrodes were positioned with the source vessel's ultra-short baseline acoustic positioning system. All positioning information was copied to the receiver vessel by radio. As the source vessel approached the receiver vessel, the receiver vessel took up receiver cable two channels at a time until there were no more channels. The data obtained with this configuration in 2007 are shown by the left-hand patch of red circles in Fig. 8. The receiver vessel then laid the cable again, east of the original cable lay, with the first channel position overlapping, as near as possible,

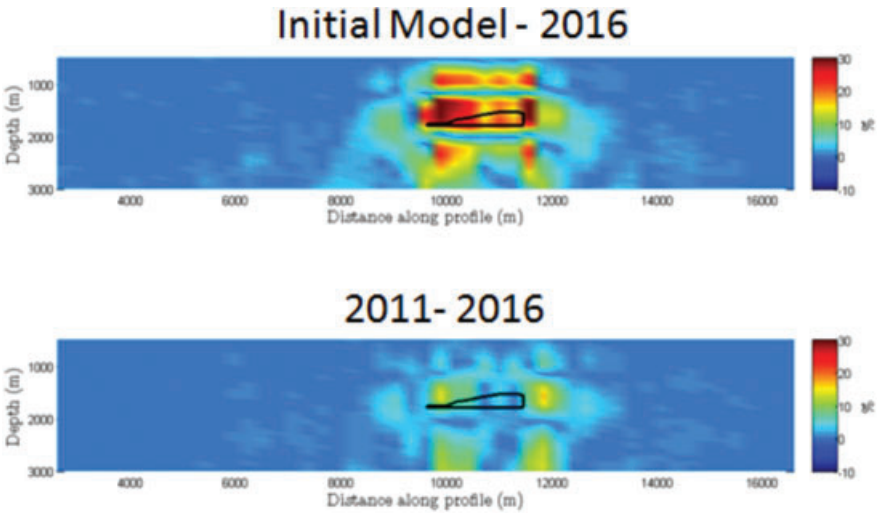

Figure 7 Relative percentage differences in inversion results, obtained by subtracting the value at the later time from the value at the earlier time, point-by-point and expressing this as a percentage of the value at the earlier time. The model reservoir is delineated by the black outline at 1700 m depth and 10 000–11 500 m on the horizontal axis.

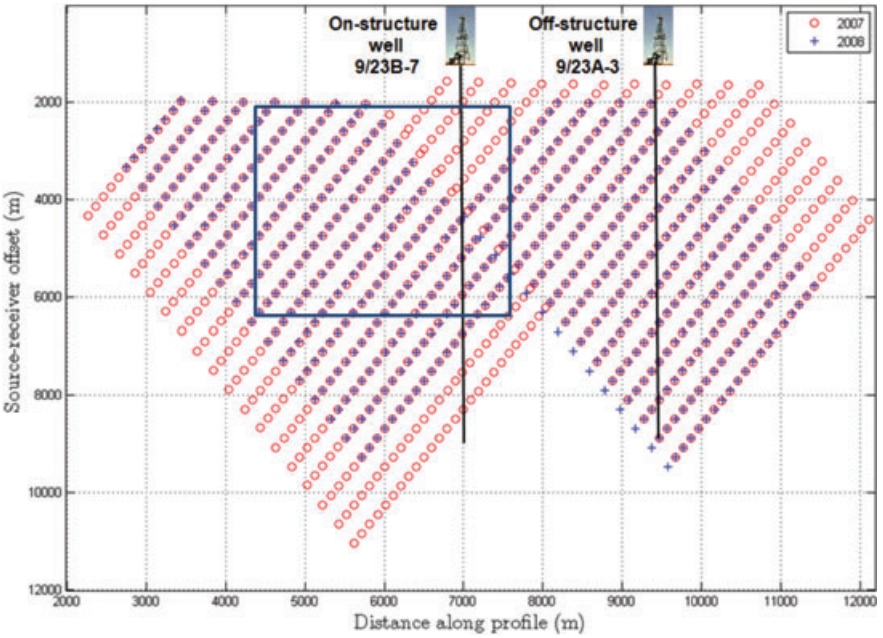

Figure 8 Showing subsurface coverage for 2007 and 2008 surveys. Horizontal axis is common mid-point number; vertical axis is source-receiver separation, or offset. Each dot represents one source-receiver pair. Red circles are 2007 data; blue crosses are 2008 data. The blue box outlines the target zone.

with the last channel position of the first cable lay. The source vessel positioned the cable and then moved to the eastern end at an offset of about 7000 m for the first record. Again the moveup between records was 400 m. The data obtained with this second cable lay are shown by the right-hand patch of red circles in Fig. 8.

The 2008 survey was essentially a repeat of the 2007 survey and the data are shown by the blue crosses in Fig. 8. Both

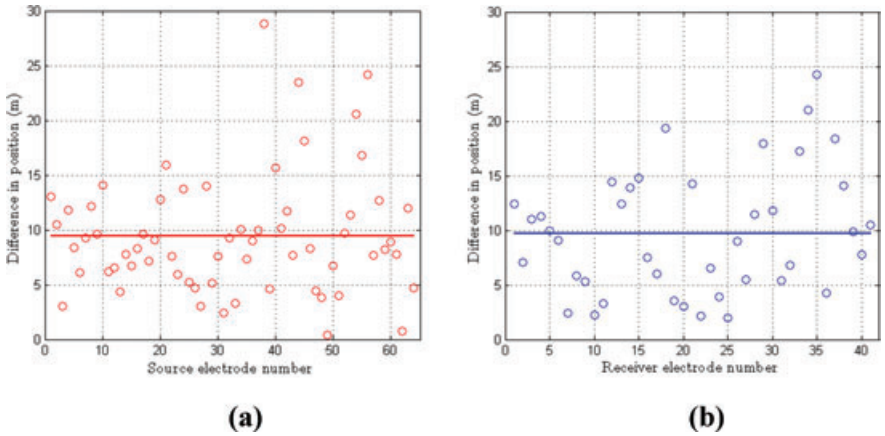

Figure 9 Showing absolute differences in positions between the 2007 and 2008 surveys of a) the source electrodes and b) the receiver electrodes.

source and receiver vessels had dynamic positioning and were able to hold their positions.

Positioning repeatability errors

The positions of the source and receiver electrodes in the 2007 and 2008 surveys were not identical, although it is not possible to see this in Fig. 8. The precision with which we were able to measure absolute positions of the vessels with GPS was about 2.5 m. The positions of the source and receiver electrodes were measured within about 2 m precision relative to the source vessel. For each source position there are two electrode positions. The receivers have electrodes at both ends and are arranged end-to-end in the cable, with a transponder at the position shared by the electrodes of adjacent receivers. Figure 9 shows the absolute differences between the 2007 and 2008 source electrode positions (Fig. 9a) and receiver electrode positions (Fig. 9b).

Optimization of source signal parameters

Propagation of the electromagnetic disturbance in the Earth is governed by the diffusion equation. An impulse decreases in amplitude and spreads out in time as it propagates. Its amplitude is approximately inversely proportional to the fifth power of the source-receiver separation, or offset, while its duration is proportional to the square of the offset (Ziolkowski 2007a,b). High-frequency energy is very much attenuated as offset increases. There is no input signal that is ideal for all offsets. The bandwidth of the pseudo-random binary sequence source signal was optimized according to the method of Ziolkowski (2007a) for different offset ranges. A pseudo random binary sequence is a signal that switches between two levels in a pseudo-random way. In our case these levels were +700 A and –700 A and polarity reversals were at pseudo-random multiples of some chosen minimum time Δt. The pseudo-random binary sequence has a flat spectrum in the frequency bandwidth $1/(N\Delta t) \leq f \leq 1/(2\Delta t)$, where f is the frequency and $N\Delta t$ is the duration of the sequence; $N = 2^n - 1$, where n is the order of the pseudo-random binary sequence. For the Harding surveys Δt was chosen to be 25 ms for short offsets, 100 ms for intermediate offsets and 200 ms for long offsets. The order of the pseudo-random binary sequence was 12 for all offsets. Source current amplitude was 700 A.

DATA PROCESSING

The two data sets were acquired with the same parameters and processed with the same processing flow. The main elements of the processing were deconvolution, offset correction and reduction of spatially-correlated noise.

Deconvolution

The deconvolution process for MTEM data is described in Ziolkowski *et al.* (2007). Transforming equation (1) to the frequency domain yields

$$V(\omega) = \Delta x_r \Delta x_s I(\omega) G(\omega) + N(\omega), \tag{3}$$

where the change of domain from time to frequency is denoted by upper case letters in place of lower-case letters and the convolution becomes a multiplication. Δx_s and Δx_r are known from the positioning of the source and receiver electrodes, respectively. A simple division by $\Delta x_r \Delta x_s I(\omega)$ would be numerically unstable, because the noise is magnified

uncontrollably at frequencies where $|I(\omega)|$ is small. Instead, following Stoffa and Ziolkowski (1983), we multiply by

$$Z(\omega) = \frac{\bar{I}(\omega)}{\Delta x_r \Delta x_s \left(|I(\omega)|^2 + \varepsilon\right)} D(\omega). \tag{4}$$

In this expression the bar denotes a complex conjugate. Multiplying top and bottom by $\bar{I}(\omega)$ leaves the operator unchanged but makes the denominator real and positive. ε is a small positive constant that prevents the noise blowing up wherever $|I(\omega)|$ is small. Note that $i(t)$ is not the pseudo-random binary sequence; it is the measured current. The filter $D(\omega)$ is the Gaussian

$$D(\omega) = \exp\left(-\left(\frac{\omega}{\omega_0}\right)^2\right), \tag{5}$$

where $\omega_0 = \pi/(2\Delta t)$ is half the Nyquist frequency.

Offset correction

A consequence of the acquisition is that the source and receiver electrodes were not in exactly the same places for the two surveys. We noted above that the impulse response is very dependent on source-receiver separation, or offset. We define the offset r as the distance between the midpoint of the source electrodes and the midpoint of the receiver electrodes. Ziolkowski (2007a,b) showed that the amplitude of the impulse response for a half-space varies inversely as the fifth power of the offset, that is, as r^{-5}. A +1% change in offset results in a –5% change in amplitude. Since all the offsets are known from the positioning data, the 2008 responses can be corrected for the offset differences, using this half-space approximation. The mis-positioning error was essentially a shift in the position of the cable and resulted in the greatest percentage error at small offsets. The correction procedure is illustrated in Fig. 10.

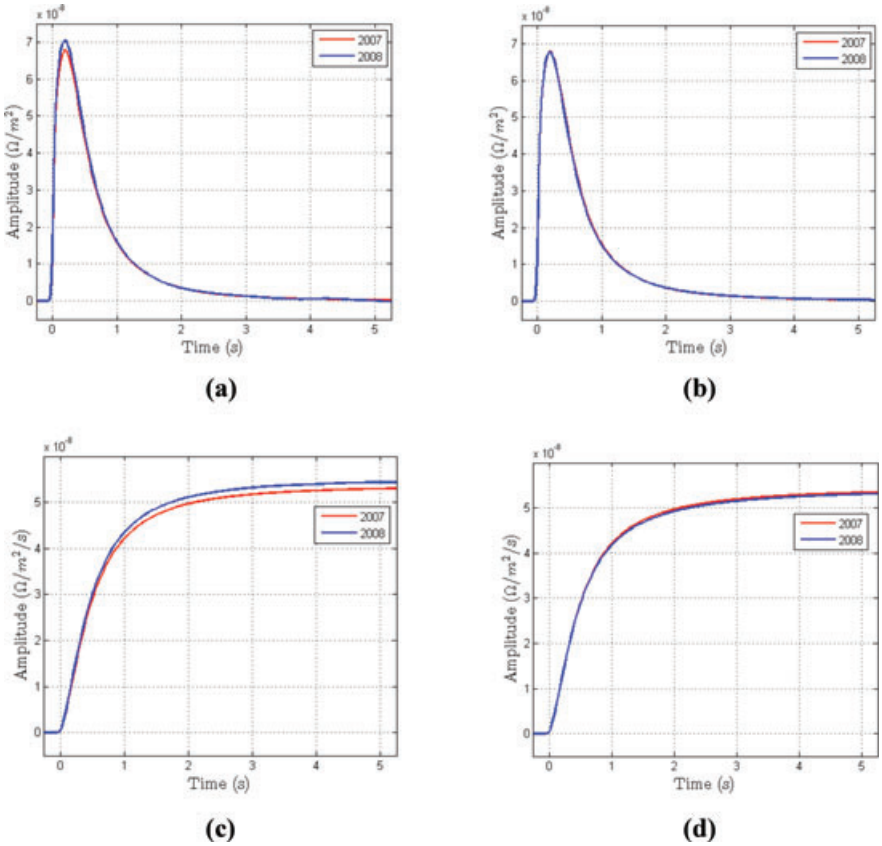

Figure 10 Example of offset correction for corresponding impulse responses after correlated noise removal. Red curve is 2007 response at 2012 m offset, blue curve is 2008 response at 1997 m offset. a) Corresponding impulse responses before offset correction; b) same as (a) but 2008 response has been amplitude corrected for offset difference; c) step responses: integrals of responses in (a); d) step responses after offset correction: integrals of responses in (c).

Figure 10(a) shows recovered impulse responses for one source position for a nominal offset of 2000 m. The 2007 offset was 2012 m and the 2008 offset was 1997 m. The peak of the 2008 response is bigger because the offset is smaller. Figure 10(c) shows the corresponding step responses, obtained by integrating the impulse responses of Fig. 10(a); the 2008 response has a noticeably larger late-time value than the 2007 response. Figure 10(b) shows the result of applying the offset amplitude correction to the 2008 impulse response: it is now nearly identical with the 2007 impulse response. Figure 10(d) shows the step responses obtained by integrating the impulse responses of Fig. 10(b): they are now almost identical. In fact, for this example, the late-time values now differ by only 0.1%.

Spatially-correlated noise removal

Various sources of electromagnetic noise exist at the bottom of the sea. For example, a reviewer has pointed out that in shallow water tidal currents and waves are a cause of noise. We checked this and found that waves and currents can cause motion of the instruments on the sea floor, particularly tilt, which creates spurious signals, especially in the magnetic field measurements (Lezaeta, Chave and Evans 2005). Lezaeta *et al.* (2005) made magnetotelluric (MT) measurements. As far as active electromagnetic surveying is concerned, MT signals are noise, in the same way that earthquake waves and microseisms are background noise for the seismic reflection method.

"Natural EM signals come from an enormous variety of processes and from sources ranging from the core of the earth to distant galaxies. Within the frequency range of interest in exploration, say 0.001–10^4 Hz, only two source regions are important. These are the atmosphere and the magnetosphere. Electrical storms in the lower atmosphere are the dominant cause of fields between 1 Hz and 10 kHz, whereas below 1 Hz the fields originate primarily in hydromagnetic waves in the magnetosphere." (Vozoff 1991).

Figure 11 shows the total noise, including MT noise, measured in the North Sea in 100 m water using the configuration shown in Fig. 3(b) with the source switched off. The spectrum has a peak between 7–8 Hz, which is probably the first Schumann resonance (typically 7.83 Hz, Madden and Thompson 1965); it also has a peak at about 0.13 Hz, which is attributed to ocean swell noise (Weitmeyer and Constable 2009).

Ziolkowski and Wright (2008) developed a method for removal of correlated electromagnetic noise that increases the signal-to-noise ratio of each data set by as much as 20 dB. The elements of the process are illustrated in Fig. 12.

Figure 12(a) shows a raw common-source gather, 250 s in length (vertical axis), with offsets (horizontal axis) increasing from 2200 m on the left to 7000 m on the right. The long-period noise is well correlated from trace to trace; the response

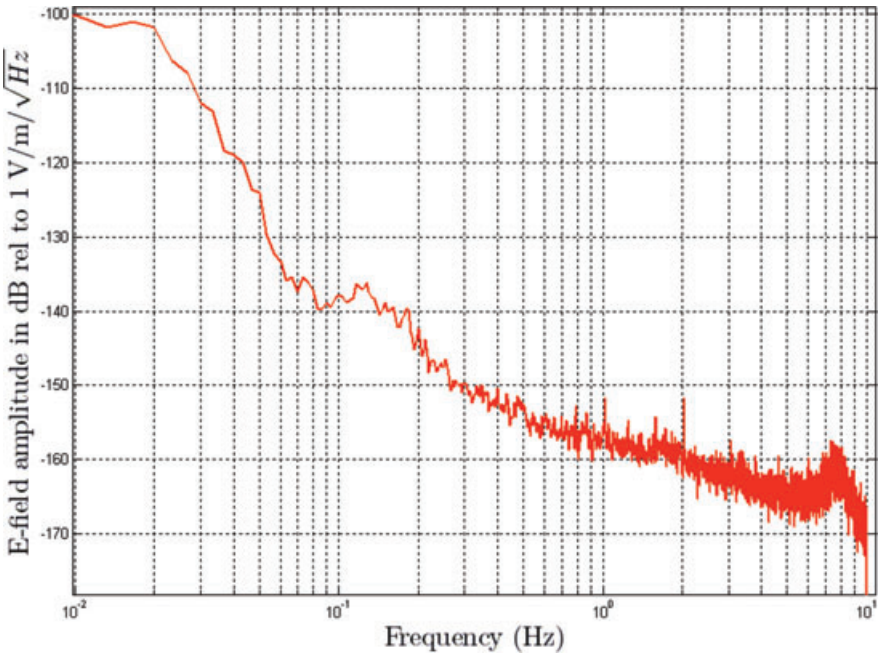

Figure 11 Estimate of noise spectrum measured in the North Sea in 2007 in water 100 m deep, with a sea-bed electric receiver.

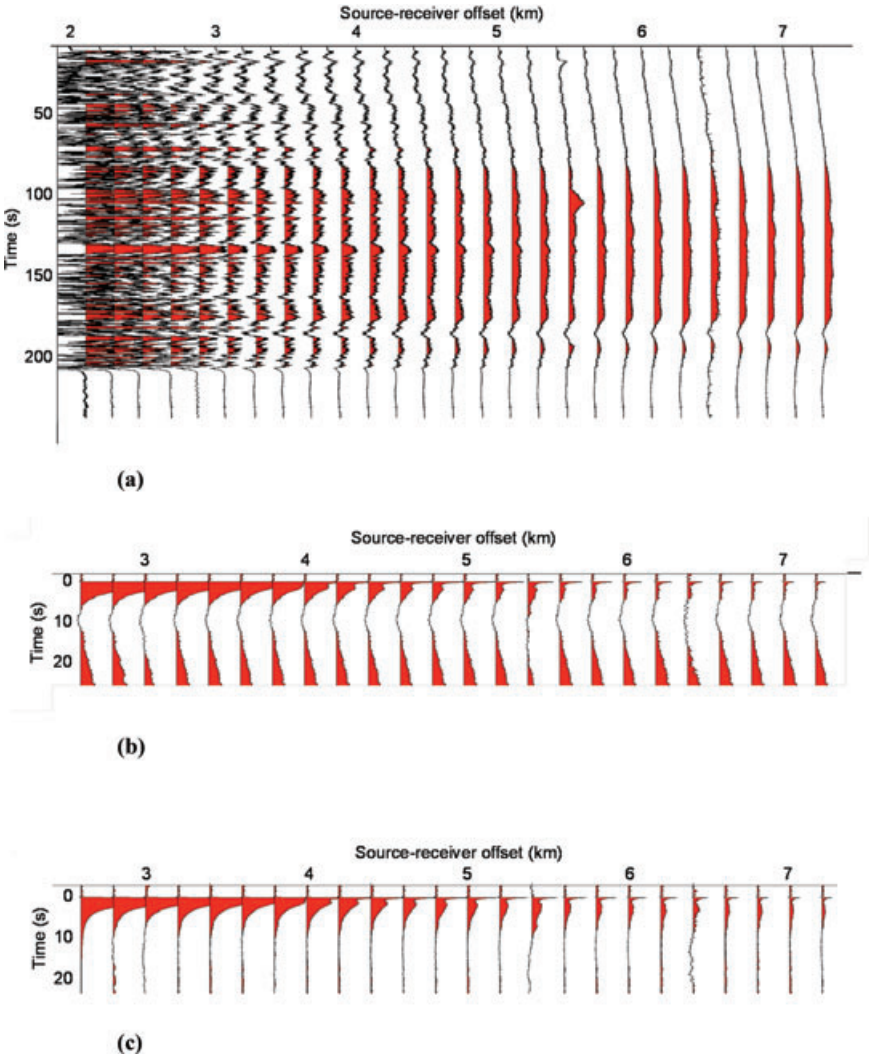

Figure 12 a) Common-source gather, 250 s in length (vertical axis), with offsets (horizontal axis) increasing from 2200 m on the left to 7000 m on the right. b) Result of deconvolving source gather for measured current, showing only 20 s of data: signal has been compressed to impulse responses but the noise remains. c) Result of subtracting estimated noise from data in (b).

to the pseudo-random binary sequence input decays dramatically from near to far offsets. Figure 12(b) shows the result of deconvolution in a 20 s window containing the impulse response: the long signal responses to the pseudo-random input current have been compressed to impulse responses but the noise remains. An estimate of the noise is obtained by subtracting the short impulse response from the nearest 250 s trace. This noise estimate is similar to the noise on the other traces. To determine the component of the noise on each subsequent trace that is correlated with this noise estimate, a Wiener filter is found for each trace that best estimates the correlated part – the noise – from this noise estimate. The noise estimated in this way on each subsequent trace is then subtracted from the trace to reveal the impulse response, as shown in Fig. 12(c). The increase in signal-to-noise ratio from Figs 12(b)–(c) is about 20 dB. This is equivalent to increasing the source current from 700–7,000 A.

The correlated noise is essentially independent of offset, whereas the signal decays dramatically with offset. The signal-to-noise ratio therefore decreases dramatically with offset. Figure 13 shows an example of the effect of correlated noise removal on a pair of impulse responses at a long offset of 6600 m. Figure 13(a) shows recovered impulse responses before noise removal; they are not identical because of the difference in the noise between 2007–2008. Figure 13(c) shows the corresponding step responses, obtained by integrating the

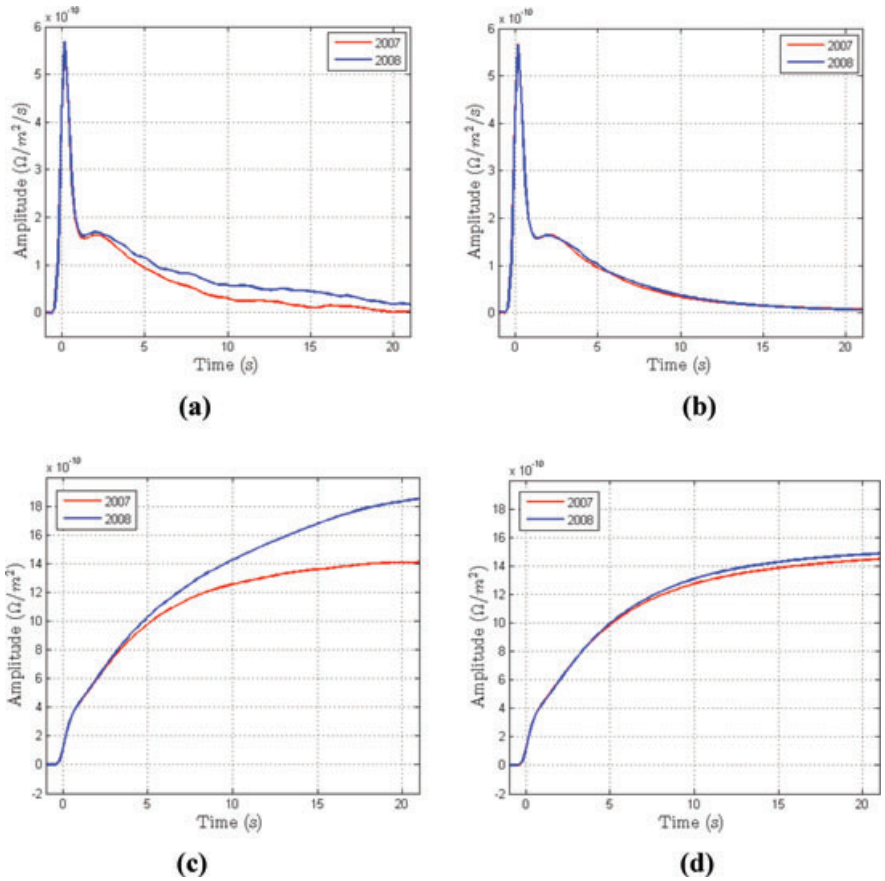

Figure 13 Example of correlated noise removal for corresponding impulse responses at an offset of 6600 m. Red curve is 2008 response, blue curve is 2007 response. a) Corresponding impulse responses before noise removal; b) same as (a) but correlated noise has been removed; c) step responses: integrals of responses in (a); d) step responses after offset noise removal: integrals of responses in (b).

impulse responses of Fig. 13(a); there is a considerable difference in the late-time value between the two responses. Figure 13(b) shows the result of applying correlated noise removal: the two responses are now nearly identical. Figure 13(d) shows the step responses obtained by integrating the impulse responses of Fig. 13(b): the late-time values now differ by only a few per cent.

RESULTS FROM THE FIELD EXPERIMENT

Repeatability

The repeatability of the transient EM data can be estimated using the well-known normalized root mean square difference between the data sets. The normalized root mean square difference (*NRMSD*) between the 2007 data a_t and 2008 data b_t is given by

$$NRMSD = \frac{200\,RMS(a_t - b_t)}{RMS(a_t) + RMS(b_t)}, \tag{6}$$

where

$$RMS(x_t) = \left(\frac{1}{N}\sum_{t=1}^{N} x_t^2\right)^{\frac{1}{2}}, \tag{7}$$

and N is the number of samples in the response.

Figure 14 shows how the impulse responses differed before (average 11.9%) and after (average 3.9%) the removal of correlated noise. 3.9% is very low. Corresponding figures for time-lapse seismic surveys are much higher; for example, Kragh and Christie (2002) quoted 18–30%. The best figure we have found is 7% (Staples *et al.* 2006). We conclude that MTEM data are at least as repeatable as time-lapse 3D seismic data.

The real MTEM data were inverted using collated multi-trace 1D isotropic inversions of CMP gathers with similar results from the 2007 and 2008 surveys. We found that unconstrained isotropic Occam inversion tended to put the reservoir too shallow. We therefore applied weak constraints. Layer

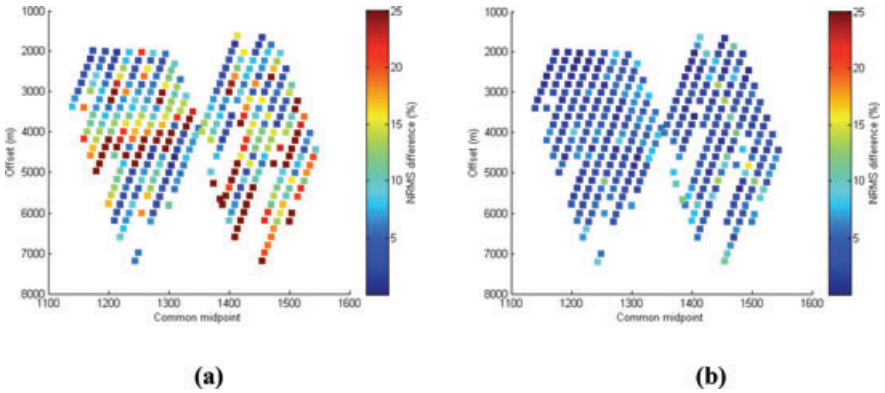

Figure 14 Normalized root-mean-square difference of impulse responses a) before and b) after offset-correction and spatially-correlated noise removal in common-midpoint (CMP) offset coordinates.

boundaries were constrained to follow seismic interfaces. The Top Balder depth across the section was taken from the wells and the seismic data and the layer below it was taken to have a thickness of 100 m and starting resistivity of 1.8 Ωm. The four other layer boundaries were taken from the seismic data but the starting resistivity in each of the other layers below the sea floor was 1.6 Ωm.

Figure 15 shows results of the constrained 1D inversion of data from the same CMP close to the position of the on-structure well for the 2007 and 2008 data. In each case the starting model is shown on the left in grey, with the final model in red. The fits of the 1D modelled data, in red, to the measured impulse responses, in blue, are shown on the right. For 2007 there were seven measured impulse responses available and for 2008 there were ten. The normalized root mean square difference for the fit of 1D synthetic to real data for this CMP for 2007 data was 7%; for 2008 it was 9%.

The time-lapse modelling study of Harding, described above, showed that the 3.9 MMbbls of production between the two surveys had a negligible impact on the EM responses. Therefore we were able to combine the data sets. Figure 16 shows the result at the same CMP as for the inversions of Fig. 15. In this case, the starting resistivity in all layers was 1.6 Ωm. The resistive reservoir stands out more clearly. Figure 17 shows the result of displaying the 1D inversions side-by-side for the whole line. The Harding reservoir is found and the edges of the inverted electrical resistor approximately define the known gas-bearing reservoir with an error of 200–400 m. This is consistent with the data acquisition geometry: 200 m receiver spacing and 400 m source spacing. Moreover the result of this inversion of the MTEM data is also consistent with the interpretation at the dry well (Fig. 2), outside the field. We were not able to fit the data without having a resistive shallow layer. It was later confirmed that there is in fact a shallow gas layer above Harding Central, which was the reason for positioning the platform away from the main structure.

CONCLUSIONS

We have shown that we are able to obtain good quality and repeatable MTEM data by repeating a 2D line across Harding. The constrained 1D inversion results from the two surveys show the Harding reservoir as a resistor, with fairly well-defined edges. There is no indication of a resistor at the dry well. We have demonstrated that the multi-transient EM method can be used for exploration and has the potential to be employed in field appraisal.

The recovered reservoir resistivies of the 1D inversions of CMP gathers are far too low, however, due to the mismatch between the 1D models and the 3D target. We would expect results to improve dramatically with 3D anisotropic inversion. This is a field waiting to be developed. To our knowledge, 3D anisotropic inversion has never been applied to full bandwidth transient EM data. Hobbs, Werthmüller and Engelmark (2009) showed that 1D isotropic inversion of synthetic transient EM data from a 1D anisotropic model failed to recover the model while anisotropic inversion was very successful and, in particular, had much better vertical resolution. Jing, Green and Willen (2008) showed, using 3D modelled anisotropic data at three frequencies (3/8, 5/8 and 7/8 Hz), that 3D anisotropic inversion of the data is feasible and gives results that are consistent with the synthetic data. Lovatini *et al.* (2009) applied 3D anisotropic inversion to both synthetic data and real conventional controlled source EM data

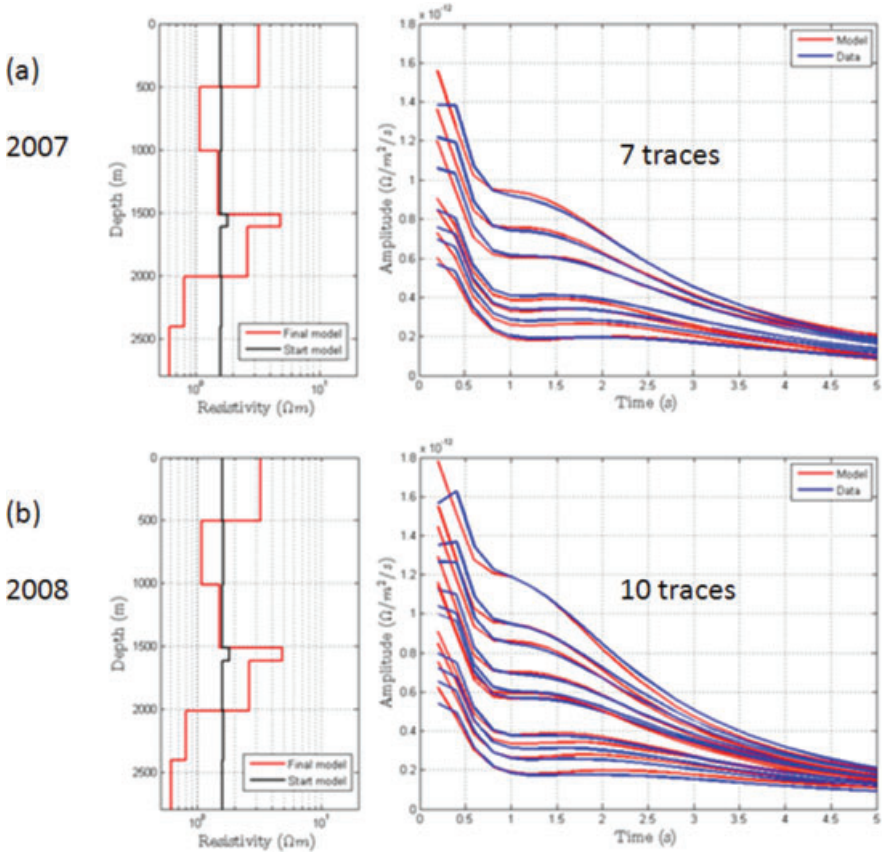

Figure 15 Example of 1D inversion of a common-midpoint (CMP) impulse response gather at the on-structure well position for a) 2007 and b) 2008 surveys. The left graph in each display shows the starting resistivity model in grey and the inverted resistivity model in red. On the right is the comparison of the real (blue) and synthetic (red) impulse responses.

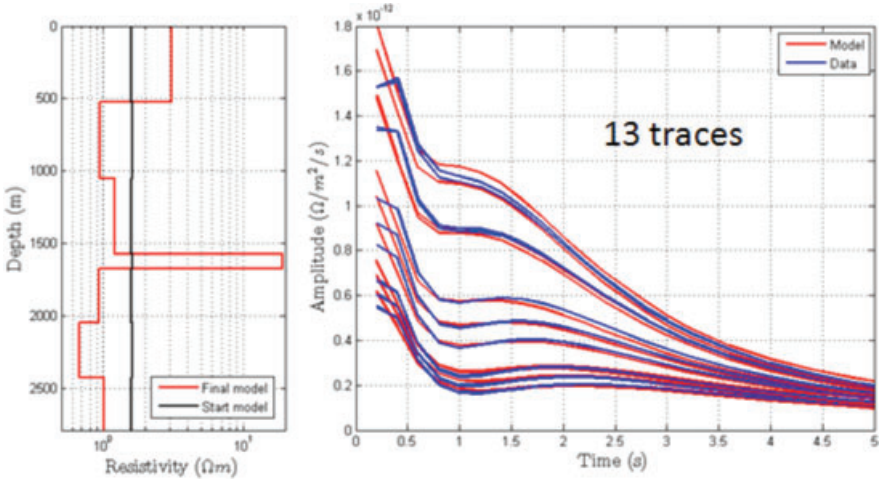

Figure 16 1D inversion of 2007 and 2008 data for a CPM at the position of the on-structure well. On the left is the 1 Ωm starting resistivity model in grey and the inverted resistivity model in red. On the right is the comparison of the real (blue) and synthetic (red) impulse responses.

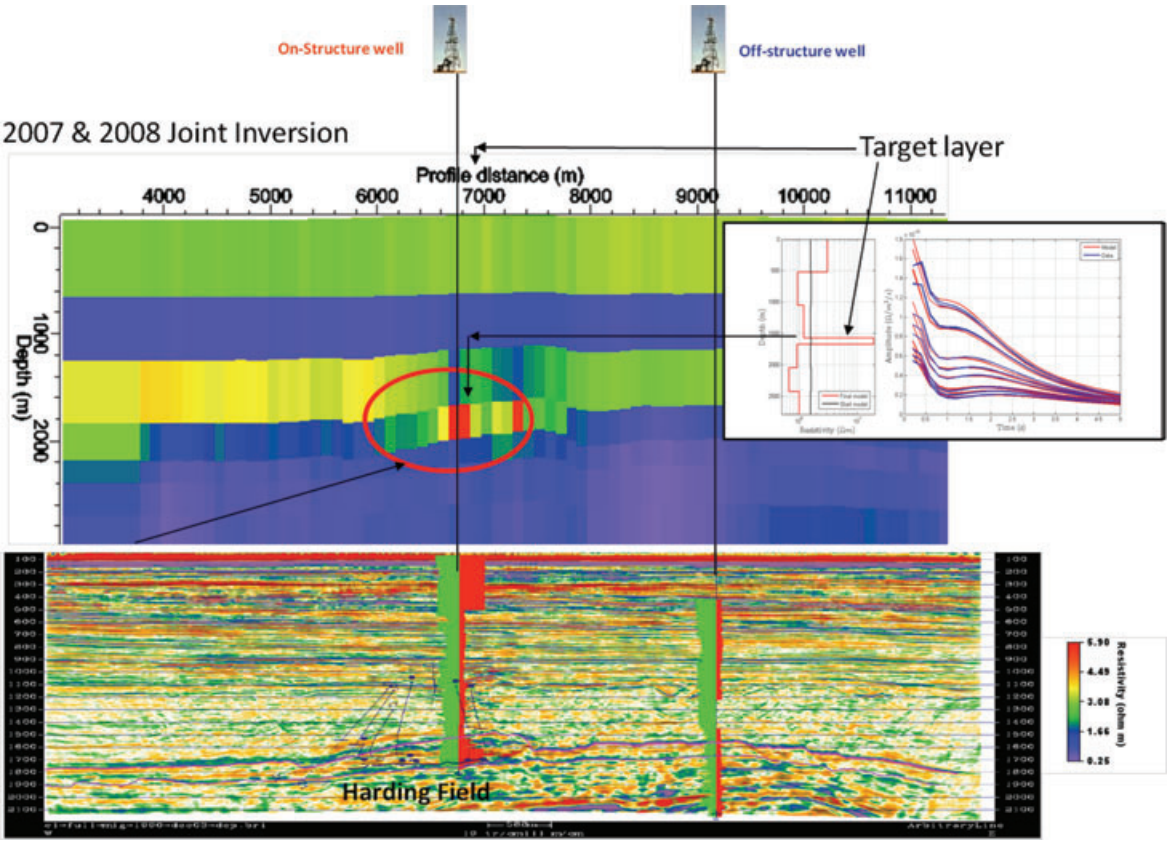

Figure 17 Inversion of the combined 2007 and 2008 survey data displayed above the depth-migrated seismic section over the Harding field, with the insert showing the inversion result at the well position.

west of Greenland at two frequencies (0.25 Hz and 0.75 Hz) and obtained very good fits to the data at those frequencies.

A key element in achieving high repeatability of the multi-transient EM data is the ability to remove spatially-correlated noise, particularly magnetotelluric noise. This gave gains in the signal-to-noise ratio of as much as 20 dB. Application of this new method to the data we acquired over Harding in 2007 and 2008 resulted in a normalized root mean square difference between the data sets of 3.9%, without any cross-matching of the data sets. This compares very favourably with figures that have been obtained in time-lapse 3D seismic surveys.

We have also demonstrated that reservoir parameters derived from detailed simulations may be converted to a resistivity model for generation of transient EM data.

In time-lapse mode the 3D transient EM modelling over Harding Central shows that the changes in reservoir resistivity caused by production of hydrocarbons from 1996–2011 would be observable, as would the changes caused by the modelled gas production, or 'blowdown', from 2011–2016. The gas cap for Harding dominates the picture after the initial oil production. The multi-transient EM method therefore has the potential to monitor the production of hydrocarbons.

The modelling defines the resolution that is required of the data to achieve the objectives that we have demonstrated. For this particular field the signal-to-noise ratio needs to be better than 40 dB to observe the major changes in production.

ACKNOWLEDGEMENTS

We thank the Department of Trade and Industry (now the Department for Business, Innovation and Skills) for supporting this research and the Harding partners (BP and Maersk) and PGS for permission to present this paper. We also thank the reviewers for their prompt reviews and very helpful comments and suggestions.

REFERENCES

Archie G.E. 1942. The electrical resistivity log as an aid in determining some reservoir characteristics. *Journal of Petroleum Technology* **5**, 1–8.

Bussian A.E. 1983. Electric conductance in porous medium. *Geophysics* **48**, 1258–1268.

Constable S.C., Parker R.L. and Constable C.G. 1987. Occam's inversion: A practical algorithm for generating smooth models from electromagnetic data. *Geophysics* **52**, 289–300.

De Witte A.J. 1957. Saturation and porosity from electric logs in shaly sands. *Oil and Gas Journal* **55**(9), 89–97.

Ellis M.H. and Sinha M.C. 2009. Investigations into the discrepancies between electro-magnetic and borehole derived resistivities in overburden sediment. 71st EAGE meeting, Amsterdam, the Netherlands, Expanded Abstracts, X021.

Glover P.W.J., Hole M.J. and Pous J. 2000. A modified Archie's law for two conducting phases. *Earth and Planetary Science Letters* **180**, 369–383.

Hacikoylu P., Dvorkin J. and Mavko G. 2006. Resistivity-velocity transforms revisited. *The Leading Edge* **25**, 1006–1009.

Hobbs B.A., Werthmüller D. and Engelmark F. 2009. Apparent anisotropy derived from transient electromagnetic Earth responses. 79th SEG meeting, Houston, Texas, USA, Expanded Abstracts, 744–748.

Hursán G. and Zhdanov M.S. 2002. Contraction integral equation method in three-dimensional electromagnetic modelling. *Radio Science* **37**, 1089. doi:10.1029/2001RS002513

Jing C., Green K. and Willen D. 2008. CSEM inversion: Impact of anisotropy, data coverage, and initial models. 78th SEG meeting, Las Vegas, Nevada, USA, Expanded Abstracts, 604–608.

Kragh E. and Christie P. 2002. Seismic repeatability, normalized rms and predictability. *The Leading Edge* **21**, 640–647.

Lezaeta P.F., Chave A.D. and Evans R.L. 2005. Correction of shallow-water electromagnetic data for noise induced by instrument motion. *Geophysics* **70**, G127–G133.

Lovatini A., Watts M.D., Umbach K.E., Ferster A., Patmore S. and Stilling J. 2009. Application of 3D anisotropic CSEM inversion offshore west of Greenland. 79th SEG meeting, Houston, Texas, USA, Expanded Abstracts, 830–834.

Madden T. and Thompson W. 1965. Low-frequency electromagnetic oscillations of the Earth-ionosphere cavity. *Reviews of Geophysics* **3**, 211.

Staples R., Stammeijer J., Jones S., Brain J., Smit F. and Hatchell P. 2006. Time-lapse (4D) seismic monitoring – Expanding applications. 2006. CSPG CSEG CWLS, Calgary, Canada, Expanded Abstracts.

Stoffa P.L. and Ziolkowski A.M. 1983. Seismic source decomposition. *Geophysics* **48**, 1–11.

Vozoff K. 1991. The magnetotelluric method. In: *Electromagnetic Methods in Applied Geophysics, Volume 2* (ed. M.N. Nabighian), pp. 641–711. SEG.

Weitemeyer K. and Constable S. 2009. Marine electromagnetic methods for gas hydrate characterization. Scripps Institution of Oceanography Cruise Report.

Wright D., Ziolkowski D. and Hall G. 2006. Improving signal-to-noise ratio using pseudo-random binary sequences in multi-transient electromagnetic (MTEM) data. 68th EAGE meeting, Vienna, Austria, Extended Abstracts, P065.

Wright D., Ziolkowski A. and Hobbs B. 2002. Hydrocarbon detection and monitoring with a multicomponent transient electromagnetic (MTEM) survey. *The Leading Edge* **21**, 852–864.

Wright D.A., Ziolkowski A.M. and Hobbs B.A. 2005. Detection of subsurface resistivity contrasts with application to location of fluids. US Patent 6,914,433.

Ziolkowski A.M. 2007a. Optimisation of MTEM parameters. International patent application no. PCT/GB2007/000843, publication WO 2007/104949.

Ziolkowski A. 2007b. Developments in the transient electromagnetic method. *First Break* **25**, 99–106.

Ziolkowski A., Hobbs B.A. and Wright D. 2007. Multitransient electromagnetic demonstration survey in France. *Geophysics* **72**, 197–209.

Ziolkowski A.M. and Wright D.A. 2008. Method for attenuating correlated noise in controlled source electromagnetic survey data. US Patent Application 12/231,118.